

# Evolution of progenitors for electron capture supernovae

Koh Takahashi, Takashi Yoshida, and Hideyuki Umeda

*Department of Astronomy, The University of Tokyo ver.2/26*

## ABSTRACT

We provide progenitor models for electron capture supernovae (ECSNe) with detailed evolutionary calculation. We include minor electron capture nuclei using a large nuclear reaction network with updated reaction rates. For electron captures, the Coulomb correction on the rates is treated and contribution of neutron-rich nuclei are taken into account in the nuclear statistical equilibrium (NSE) composition. We calculate the evolution of the most massive super asymptotic giant branch stars and show that these stars undergo off-center carbon burnings and form ONe cores at the center. These cores get heavier up to the critical mass of  $1.367 M_{\odot}$  and keep contracting even after the initiation of O+Ne deflagration. Though inclusion of minor electron capture nuclei causes convective URCA process at the contraction phase, such process will have minor effect on the evolution. On the other hand, electron captures by neutron-rich nuclei in the NSE region have more significant effect. Also, we discuss the uniqueness of the critical core mass for ECSNe and the effect of mass loss on the plausibility of our models for ECSN progenitors.

*Subject headings:* nuclear reactions, nucleosynthesis, abundances, — stars: evolution — stars: interiors — supernovae: general

## 1. Introduction

Electron capture supernova (ECSN) is a quite distinct class in core collapse supernova (CCSN). While an ordinary CCSN is considered to be triggered by a collapse of an Fe core, which is located at the center of the star with an onion-like compositional structure, a progenitor of an ECSN is a super asymptotic giant branch (SAGB) star that has a core mainly consists of oxygen and neon, surrounded by a thin helium shell and diffuse hydrogen envelope (Nomoto 1987). In an ONe Chandrasekhar mass core, electron capture reactions on  $^{24}\text{Mg}$  and  $^{20}\text{Ne}$  heat the surroundings. As a result, O and Ne burning ignites at the center and generates energy, and O+Ne deflagration propagates outward. However, the released

energy is too small to explode the highly bound core (Miyaji et al. 1980). Further electron capture reactions in the central NSE region (Nuclear Statistical Equilibrium) accelerate core contraction. Finally, a proto-neutron star forms and the star ends up as a weak type II supernova (Kitaura et al. 2006).

The most distinct point of the progenitor may be its contrasting structure of a highly concentrated core and a diffuse envelope. With a progenitor model of an ECSN (Nomoto 1987), a hydrodynamical simulation by Kitaura et al. (2006) showed that the delayed explosion powered by neutrino heating takes place even in a one-dimensional calculation, and the successful explosion is confirmed by recent multi-dimensional calculations as well (Janka et al. 2012). From these self-consistent calculations, properties of ECSNe such as nucleosynthesis (Wanaajo et al. 2011, 2013) have been studied.

Not only for a theoretical aspect, but also for observations, a model of ECSN has important suggestions. Some low luminosity SNe, e.g., SN1997D (Turatto et al. 1998), SN2005cs (Pastorello et al. 2006, 2009), can be explained by the explosion model of an ECSN which has a low explosion energy and synthesizes small amount of  $^{56}\text{Ni}$ . Also observed peculiar compositions in the well-known Crab nebula, such as abundant He and less abundant C and O, indicate that the Crab supernova SN1054 arose from a collapse of a SAGB star. (Nomoto et al. 1982). Type IIn SN, which is a SN explosion enshrouded by a dense circumstellar medium, can be explained by an ECSN as well as a CCSN from very massive star that has experienced an intense mass loss phase. Recently, a progenitor of a dust-enshrouded transient SN2008S is found in a pre-explosion image (Botticella et al. 2009) and it would have a mass of  $\sim 10 M_{\odot}$ , which is a plausible mass for an ECSN progenitor.

However, there has not been a consistent progenitor calculation from zero age main sequence (ZAMS) to collapse because of the numerical difficulties to calculate the full evolution of SAGB stars. The main difficulties are off-center C burning, thermal pulses, contraction of a highly degenerate core, calculation of electron captures, and propagation of deflagration. These phases had been separately studied by several authors.

The theoretical work on a collapsing ONe core was initiated by Nomoto and collaborators in 80's (Miyaji et al. 1980; Miyaji & Nomoto 1987; Nomoto 1984, 1987). Miyaji et al. (1980) investigated the effect of electron capture on  $^{24}\text{Mg}$  and  $^{20}\text{Ne}$  and showed that these effects can be summarized as follows: Firstly, reduction of the electron mole fraction induces core contraction. Secondly, reduction of the electron mole fraction reduces the Chandrasekhar mass. And finally, electron capture affects the energy equation by both endothermic and exothermic way. Moreover, Nomoto (1987) followed the core evolution either after the initiation of O+Ne deflagration using a He star model and provided the progenitor model for an ECSN. This model has been the only one that can be used in an explosion simulation. In 90's,

non-explosive evolutionary calculation of solar-metal SAGB stars was investigated by García-Berro and collaborators (García-Berro & Iben 1994; Ritossa et al. 1996; García-Berro et al. 1997; Iben 1997; Ritossa et al. 1999). Non-solar metallicity (Gil-Pons et al. 2005; Siess 2007), as well as detailed physics such as overshooting (Gil-Pons et al. 2007) and thermohaline convection (Siess 2009) are considered in recent studies. An off-center carbon burning and thermal pulses, which require a high cost calculation, were extensively investigated by Siess (2006, 2010). The contraction phase of an ONe core was investigated by recent works as well, concerning the different nuclear reaction rates (Hashimoto et al. 1993), different convective assumptions (Gutiérrez et al. 1996), and different compositions (Gutiérrez et al. 2005). These simulations stopped at the ignition of O burning and the continuous deflagration phase had not been calculated.

Thus the main purpose of this work is to calculate a progenitor model for an ECSN from a detailed stellar evolutionary simulation. The calculation treats its main sequence phase, which is omitted in the work by Nomoto (1987). Also an off-center C burning phase, which is one of the important improvement in the evolutionary theory for SAGB stars, is followed in detail. Using a large nuclear reaction network, we include minor nuclei that are synthesized during C burning phase and additional electron capture reactions on these nuclei are treated with the Coulomb correction on rates. Updated nuclear reaction rates, especially the new electron capture rate for the NSE composition by Juodagalvis et al. (2010), is taken into account. The growth of an ONe core mass is assumed to be a result of a stationary helium burning. This enables us to avoid numerical difficulties on shell He burning and to investigate the full evolution of an ONe core.

The critical core mass for ECSNe, with which an ONe core can no longer exist as a stable object because of the initiation of electron capture reactions, is considered to be a uniquely determined quantity and the value by Nomoto (1987) is used for estimates of the initial mass range for ECSNe (Siess 2007; Poelarends et al. 2008; Pumo et al. 2009). However, the uniqueness on various parameter settings has not been confirmed yet owing to lack of calculations. Moreover, update of both numerical prescriptions and physical effects such as diffusive convective mixing and the Coulomb correction on electron capture rates possibly affect the value. Thus investigation on the parameter dependence of the critical core mass for ECSNe is intended in this work as well.

We report stellar evolution of the most massive SAGB stars with solar composition from its main sequence through ONe core contraction, and further deflagration phase in which the central NSE region extends outward. In the next section, the method of calculation and input physics are explained. The evolutionary results from ZAMS phase to the formation of the ONe core are presented in § 3.1., and core contraction including the propagation of NSE

front are explained in § 3.2. Discussions and conclusions are given in § 4.

## 2. Methods

The code was modified from Yoshida & Umeda (2011) (hereafter, referred as Y&U11) in order to calculate the late phase of ONe core evolution. The mixing length was set to be 1.5 times pressure scale height. Other assumptions and description of the code is given in Umeda et al. (2012). In the followings, we explain other modified points.

### 2.1. Spatial resolution

Mesh points are automatically replaced to achieve required resolutions for calculations of stellar structures. Different conditions are set for different environments as well as different evolutionary phases. Especially, for the case of propagation of shell C burning, which requires careful treatment of mesh refining,

- (i)  $|\Delta \log P| < 0.05$
- (ii)  $|\Delta \log T| < 0.1$
- (iii)  $|\Delta \log r| < 0.1$
- (iv)  $\sqrt{(\Delta L_r)^2 / L_r^2} < 0.1$
- (v)  $\Delta M_r / M < 10^{-4}$

are taken as the constraints, where  $\Delta f$  means the difference of  $f$  between two mesh points and symbols have their usual meanings.

### 2.2. Nuclear reaction network

We include 300 species of nuclei in a reaction network from n, p to Br. That is used for the calculation of distribution evolution of chemical composition and also nuclear energy generation. Newly added nuclei from Y&U11 (see also Yoshida et al. (2013)) are shown in Fig. 1.

When the temperature exceeds the value of  $5.0 \times 10^9$  K, the composition in the region is assumed to achieve the NSE composition and the composition is used for the calculation

of the thermodynamical quantities and nuclear generation rate. In a NSE region in a highly dense ONe core, both density and electron mole fraction changes its value in wide ranges of ( $9.0 \lesssim \log \rho \lesssim 11.0$ ) and ( $0.25 \lesssim Y_e \lesssim 0.5$ ). In order to calculate the NSE composition consistently in such a wide parameter space, 3091 nuclei are treated for calculations of NSE abundance (Fig. 2). For electron capture reactions in the NSE region, we applied the rate by Juodagalvis et al. (2010) which takes into account roughly 2700 nuclei including very neutron-rich and heavy ones with screening corrections. Though the contributions from positron capture and decay as well as  $\beta^-$ -decay in the NSE region may affect the stellar evolution, we omit these effects because of the lack of data tables.

### 2.3. Convective criterion and diffusive mixing approximation

In our code, convective mixing is treated as a diffusive process, and mixing beyond the convective boundaries such as overshooting is not treated. Convective boundaries are determined by the Schwarzschild criterion, and semi-convective diffusion coefficient by Spruit (1992) is also applied, thus

$$D_{mix} = \begin{cases} \frac{1}{3}ul_{cv} & \text{for } \nabla_{rad} - \nabla_{ad} > \min(0, \frac{\phi}{\delta}\nabla_{\mu}) \\ f_{sc}D_{therm}\frac{\nabla_{rad}-\nabla_{ad}}{\frac{\phi}{\delta}\nabla_{\mu}} & \text{for } 0 < \nabla_{rad} - \nabla_{ad} \leq \frac{\phi}{\delta}\nabla_{\mu}, \end{cases} \quad (1)$$

where  $u$  and  $l_{cv}$  are convective velocity and scale length determined by the mixing length theory, respectively.  $D_{therm} \equiv \frac{1}{C_p\rho} \frac{4acT^3}{3\kappa\rho}$  is the thermal diffusivity, and  $f_{sc}$  is a free parameter taken as 0.3 according to Umeda & Nomoto (2008). In order to take into account the effect of degeneracy of electrons both into the criterion and the coefficient of convective mixing, we define

$$\frac{\phi}{\delta}\nabla_{\mu} \equiv \frac{1}{\delta}(\phi_i\nabla_i + \phi_e\nabla_e) \quad (2)$$

by extending the work in Kato (1966), where

$$\delta \equiv -\frac{\partial \ln \rho}{\partial \ln T}, \phi_i \equiv \frac{\partial \ln \rho}{\partial \ln \mu_i}, \phi_e \equiv \frac{\partial \ln \rho}{\partial \ln \mu_e}, \nabla_i \equiv \frac{d \ln \mu_i}{d \ln P}, \nabla_e \equiv \frac{d \ln \mu_e}{d \ln P}. \quad (3)$$

Note that thermohaline convection which would take place in a region of  $\frac{\phi}{\delta}\nabla_{\mu} < 0$  is not treated for the sake of simplicity.

## 2.4. Electron capture and $\beta^-$ -decay

### 2.4.1. The energy equation

In a dense ONe core with density  $> 10^9$  g/cm<sup>3</sup>, the energy release by electron capture and  $\beta^-$ -decay of C burning products becomes important in the energy equation. The divergence of the energy flux  $L_r$  in the stellar equation is written as

$$\frac{dL_r}{dM_r} = \epsilon_n - \epsilon_\nu + \epsilon_g + \epsilon_{weak} + \epsilon_{mix}, \quad (4)$$

$$\epsilon_g \equiv -T \left( \sum_k \frac{ds_k}{dt} \right) \quad (5)$$

where  $s_k$  is the specific entropy for the  $k$ -th particle: nuclei, electrons, and photons (Miyaji et al. (1980), see also Ritossa et al. (1999)).  $\epsilon_n$  and  $\epsilon_\nu$  are the nuclear energy generation rate and the neutrino energy loss rate due to processes other than electron capture and  $\beta^-$ -decay respectively.  $\epsilon_{weak}$  is the energy generation rate of electron capture and  $\beta^-$ -decay, and  $\epsilon_{mix}$  represents a cooling term owing to the work by convection (Couch & Arnett 1975; Iben 1978). For radiation, the chemical potential is assumed to vanish, while the one of nuclei is ignored up to the achievement of NSE. For electrons, the chemical potential affects the energy equation through both  $\epsilon_{weak}$  and  $\epsilon_{mix}$ . Here we omit the description of other weak processes such as positron capture and  $\beta^+$ -decay because of small effects of these reactions.

The energy generation rate of both electron capture and  $\beta^-$ -decay consists of three terms: mass difference, neutrino emission, and chemical potential excluding subatomic energy of relevant particles (Miyaji et al. 1980). Since we ignore the chemical potential of nuclei in the energy term, the total rate becomes

$$\epsilon_{weak} = \sum_j (\Delta m_j c^2 \pm \langle E_{\nu,j} \rangle - \mu_e) \frac{dn_{e,weak,j}}{dt} \quad (6)$$

where  $\Delta m_j$  is the mass difference between parent and daughter nuclei,  $\langle E_{\nu,j} \rangle$  is the mean energy of emitted neutrino,  $\mu_e$  is the chemical potential of electron, and  $\frac{dn_{e,weak,j}}{dt}$  is a time derivative of a specific electron number density owing to the  $j$ -th electron capture or  $\beta^-$ -decay, respectively. The sign of the neutrino energy is taken positive for electron capture and is taken negative for  $\beta^-$ -decay. The specific electron number density changes according to

$$\frac{dn_{e,weak,j}}{dt} = \mp \lambda_j n_j \quad (7)$$

where  $n_j$  denotes the specific number density of the  $j$ -th nucleus, and the sign of the reaction rate of electron capture or  $\beta^-$ -decay,  $\lambda_j$ , is taken negative for electron capture and is taken positive for  $\beta^-$ -decay, so that the emission of neutrino should always take some energy away.

According to Iben (1978), we define

$$\epsilon_{mix} = \frac{\partial \mu_e}{\partial r} F_e(M_r) \quad (8)$$

where  $F_e(M_r)$  is the flux of electrons and is defined as

$$F_e(M_r) = (4\pi r^2 \rho) D_{mix} \frac{\partial n_e}{\partial M_r}. \quad (9)$$

Practically, the electron flux is calculated explicitly in our code, integrating the result of the chemical mixing, thus,

$$(4\pi \rho r^2) F_e = \int_0^{M_r} \frac{dn_{e,mix}}{dt} dM_r \quad (10)$$

where  $\frac{dn_{e,mix}}{dt}$  is a time derivative of a specific electron number density owing to chemical mixing. In this expression, the energy loss vanishes at the boundaries of the convective region where the net flow of electrons should be zero.

#### 2.4.2. Correction for the reaction rate of electron capture and $\beta^-$ -decay

The Coulomb screening for the electron capture rate (Couch & Loumos 1974; Gutiérrez et al. 1996; Juodagalvis et al. 2010) is taken into account in our code. Originally, the rate of the electron capture of  $j$ -th nucleus  $\lambda_{ec,j}$  is written as

$$\lambda_{ec,j} = \frac{1}{\pi^2 \hbar^3} \sum_{states} \int_{\epsilon_j^0}^{\infty} p_e^2 \sigma_{ec,j} \frac{1}{1 + \exp(\frac{\epsilon_e - \mu_e}{kT})} d\epsilon_e \quad (11)$$

where  $\sigma_{ec,j}$  is the electron capture cross section and  $\epsilon_j^0$  is the threshold energy of the reaction (Juodagalvis et al. 2010). This equation implies that  $\lambda_{ec,j}$  rapidly increases when  $\mu_e$  exceeds  $\epsilon_j^0$ , since electrons obey the Fermi-Dirac statistics. In highly dense regions, the equation of state of nuclei should include the Coulomb correction, and this affects the pressure, the entropy and also the chemical potential owing to the change of the Helmholtz energy. Because the chemical potential depends on a proton number  $Z$ , change in  $Z$  through the electron capture  $(A, Z) + e^- \rightarrow (A, Z - 1) + \nu_e$  will change the threshold energy of the reaction by the amount

$$\Delta \epsilon_{ec}^0 = \mu(Z - 1) - \mu(Z), \quad (12)$$

$$\mu(Z) = -kT \left( \frac{Z}{\bar{Z}} \right) \left\{ \Gamma_z \left[ 0.9 + c_1 \left( \frac{\bar{Z}}{Z} \right)^{1/3} + c_2 \left( \frac{\bar{Z}}{Z} \right)^{2/3} \right] + \left[ d_0 + d_1 \left( \frac{\bar{Z}}{Z} \right)^{1/3} \right] \right\} \quad (13)$$

where  $\Gamma_z = Z^{2/3} \bar{Z}^{4/3} \frac{e^2}{a_i k T}$ ,  $a_i = (\frac{3}{4\pi n_i})^{1/3}$  is the Coulomb coupling parameter for  $Z$  nucleus,  $\bar{Z}$  is the mean charge of ions, and the four constants are  $c_1 = 0.2843$ ,  $c_2 = -0.054$ ,  $d_0 = -9/16$ , and  $d_1 = 0.460$  respectively (DeWitt et al. 1973). Therefore the effective threshold energy becomes

$$\epsilon_{ec,eff}^0 = \epsilon_{ec}^0 + \Delta\epsilon_{ec}^0. \quad (14)$$

We assume that the energy distribution function for degenerate electrons does not change its shape in a small difference in electron density. Thus to take into account the effect of the Coulomb correction, we first evaluate the effective electron density that reproduces the effective chemical potential as the corrected Fermi energy,

$$\epsilon_{F,eff} = \epsilon_F - \Delta\epsilon_{ec}^0 \quad (15)$$

$$\equiv \mu_{e,eff}((\rho Y_e)_{eff}). \quad (16)$$

Then the reaction rate with effective electron density and fixed temperature is applied as the corrected electron capture rate,

$$\lambda_{ec,j,eff} \equiv \lambda_{ec,j}((\rho Y_e)_{eff}, T). \quad (17)$$

Since  $\Delta\epsilon_{ec}^0$  is positive, this correction increases the effective threshold energy, reduces the effective Fermi energy, and thus reduces the rate of electron capture.

The same correction is also applied to  $\beta^-$ -decay. In the case of  $(A, Z) \rightarrow (A, Z + 1) + e^- + \bar{\nu}_e$ , change in the threshold  $\Delta\epsilon_{bd}^0$  is given as

$$\Delta\epsilon_{bd}^0 = \mu(Z + 1) - \mu(Z) \quad (18)$$

which takes negative value and reduces the threshold energy. For  $\beta^-$ -decay, the decay rate is correlated to the number of unfilled states of electron in which the kinetic energy is between the threshold energy and the chemical potential, i.e.,  $\mu_e < \epsilon_e < \epsilon_{bd,eff}^0$ . Therefore, the decrease of the effective threshold energy reduces the reaction rate of  $\beta^-$ -decay as well as electron capture.

## 2.5. An approximate treatment of core growth

After the completion of carbon burnings in a forming ONe core, we assumed a constant core mass growth in order to avoid high cost calculation of shell helium burning, and we assumed that the envelope will remain and shell He burning will continue until core collapse. The radiative-zero approximation was applied to the edge of the core as boundary conditions.



Under this assumption, three rates,  $1.0 \times 10^{-5} M_{\odot}/\text{yr}$ ,  $1.0 \times 10^{-6} M_{\odot}/\text{yr}$ , and  $1.0 \times 10^{-7} M_{\odot}/\text{yr}$  are taken as the core growth rate. The middle one of  $1.0 \times 10^{-6} M_{\odot}/\text{yr}$  will be the most typical rate as the core growth from shell helium burning. This rate is consistent with the work by Nomoto (1987) in which the steady helium burning is assumed, and also with recent study by Siess (2010) and Poelarends et al. (2008) in which the TP phase is calculated. The results shown in § 3 are taken from the case of this typical rate.

## 2.6. Late phase of core evolution

When the time scale of core evolution becomes shorter than that of convection, the well-known mixing length theory (Böhm-Vitense 1958) which assumes a stationary convection becomes invalid. In order to determine the temperature gradient in such cases, the time dependent mixing length theory formulated by Unno (1967) is adopted in our calculation. In this scheme, two differential equations on time for convective velocity  $v_{cv}$  and temperature fluctuation  $\Delta T$  are given as

$$\left(\frac{d}{dt} + \frac{v_{cv}}{l_{cv}/2}\right)v_{cv} = \frac{\Delta T}{2\rho T} \left(\frac{\partial \log \rho}{\partial \log T}\right)_P \frac{dP}{dr}, \quad (19)$$

$$\left(\frac{d}{dt} + \frac{v_{cv}}{l_{cv}/2}\right)\Delta T = \frac{v_{cv}}{l_{cv}/2} \left(\frac{l_{cv}}{2H_P}\right) T (\nabla - \nabla_{\text{ad}}) \quad (20)$$

where  $\nabla - \nabla_{\text{ad}}$  represents the excess of temperature gradient compared with the adiabatic gradient. Following Nomoto (1984), we take the length scale of time dependent mixing  $l_{cv}$  as the smaller one among the radial distance and the local mixing length. The convective energy flux  $F_{cv}$  is written as

$$F_{cv} = c_P \rho \Delta T u \quad (21)$$

where  $c_P$  is the specific heat at constant pressure. Then identical to the mixing length theory, equations of total luminosity

$$L_r = L_{\text{rad}} + 4\pi r^2 F_{cv}, \quad (22)$$

$$L_{\text{rad}} = \frac{16\pi a c G M_r T^4}{3\kappa P} \nabla \quad (23)$$

are solved to get the temperature gradient.

As the timescale of evolution decreases and becomes comparable with the free-fall timescale, the assumption of hydrostatic structure becomes invalid. In this work, an inertia term is included in the equation of motion and also in the radiative temperature gradient

(Heger et al. 2000) as

$$\frac{dP}{dM_r} = -\frac{GM_r}{4\pi r^4} \left[ 1 + \frac{r^2}{GM_r} \frac{\partial^2 r}{\partial t^2} \right], \quad (24)$$

$$\nabla_{rad} = \frac{3\kappa PL_r}{16\pi acGM_r T^4} \left[ 1 + \frac{r^2}{GM_r} \frac{\partial^2 r}{\partial t^2} \right]^{-1}. \quad (25)$$

### 3. Results

We calculated the evolution of 10.4-11.2  $M_\odot$  stars with a metallicity of  $Z=0.02$ , from ZAMS to O+Ne deflagration for 10.4-10.8  $M_\odot$  models and from ZAMS to off-center Ne ignition for 11.0, 11.2  $M_\odot$  models. Figures 3 and 4 show the time evolution in the HR diagram, and in the central density-temperature plane, respectively. In Figure 4, spikes are shown at  $\rho_c \sim 10^8$  g/cm<sup>3</sup> for both 11.0 and 11.2  $M_\odot$  models, representing off-center neon ignitions. In our calculation, the minimum initial mass for Ne ignition is 11.0  $M_\odot$  and the CO core mass is 1.35  $M_\odot$ . A star with a larger initial mass than this critical mass will form an Fe core and end up as a normal CCSN (Nomoto & Hashimoto 1988). Since evolutionary properties of both 10.4 and 10.6  $M_\odot$  are similar to 10.8  $M_\odot$ , here we mostly show results of a 10.8  $M_\odot$  star, which has the largest core in these less massive stars and provides the most plausible progenitor model for an ECSN.

The minimum mass for Ne ignition  $\sim 11 M_\odot$  is large compared with other recent evolutionary calculations (Poelarends et al. 2008; Pumo et al. 2009). This is because our calculations do not take into account the effect of additional mixing such as overshooting. If an exponentially decreasing diffusion (Herwig 2000) is treated, our calculation shows that this minimum mass is reduced by  $\sim 2 M_\odot$  with an overshooting parameter of  $f_{\text{over}} = 0.02$ . This behavior is quite consistent with the calculation by Siess (2007). In fact, inclusion of overshooting importantly changes the relation between initial masses and He core masses. While this severely affects an estimation of an initial mass range for ECSNe, effects on evolutionary results of progenitor calculation are much more less. Especially, due to a lack of observational constraints, most evolutionary calculations for massive stars only take into account the overshooting before core C burning stages (Hirschi et al. 2004; Limongi & Chieffi 2006). In this case, our results on the progenitor evolution becomes fully consistent with these calculations.

### 3.1. Pre SAGB evolution

In this section, we summarize the evolutionary results of a  $10.8 M_{\odot}$  star from its ZAMS phase to the completion of the dredge-out, or emergence of convective regions which surrounds the ONe core. Figure 5 shows the time evolution of convective regions.

#### 3.1.1. *The hydrogen burning stage*

The duration of core hydrogen burning is  $1.74 \times 10^7$  yr. In this stage, convection develops in the central region due to the luminosity generated by the CNO-cycle. Core hydrogen burning continuously shifts to shell hydrogen burning as the central hydrogen burns out, while the H-depleted core contracts and is heated up by the release of the gravitational energy. The increasing luminosity in the outer shell burning region expands and cools the envelope. As the opacity increases, the convectively unstable region emerges at the surface. The base of the convective region extends inward, then the star becomes a red giant. When the first dredge-up episode occurs,  $^{14}\text{N}$ , the second main product of the CNO-cycle, is dredged up to the surface. Surface composition of these isotopes at the end of this episode are summarized in Table 1.

#### 3.1.2. *The helium burning stage*

When the central density and temperature reach  $\log \rho_c = 3.50$  and  $\log T_c = 8.16$ , core helium burning takes place. The luminosity of the shell hydrogen burning decreases, and the base of the convective envelope retreats outward in mass. The whole region of the hydrogen envelope becomes convectively stable, and the star enters into a blue-loop in the HR diagram. The core helium burning phase continues  $2.76 \times 10^6$  yr, followed by shell helium burning after core helium depletion. Since the large luminosity by shell helium burning expands and cools the hydrogen burning layer, shell hydrogen burning dies out. This luminosity re-heats the envelope and convection arises in the envelope. The star becomes an AGB star, in which the partially-degenerate CO core has formed, surrounded by the helium burning shell. At the center of the core, the ratio of mass fractions of oxygen and carbon becomes  $X(\text{C})/X(\text{O}) = 0.5728$ .

### 3.1.3. The carbon burning stage

In the partially-degenerate CO core, an off-center C flashes take place. In our calculation, the first two flashes ( $C_1$  &  $C_2$  in Fig. 6) arise near the center and last seven flashes burn outward (from  $C_3$  to  $C_9$  in Fig. 6). These C flashes transform core carbon into neon and other intermediate mass nuclei. After the end of the sixth C burning, the second dredge-up reduces the mass of the helium layer, and the extent of the second dredge-up is smaller than lower massive stars. These results are consistent with other calculations (Siess 2006, 2007). Figure 7 shows the evolution of the core structure in terms of  $\beta_e$ , the ratio of electron pressure to the total pressure, temperature, and density at five different stages: disappearance of convective core helium burning (1a), commencement of the first shell carbon burning (1b), ignition at the center of the core (1c), ignition of the eighth C burning (1d), and occurrence of the dredge-out (1e).

In advance of the off-center C ignition, the gravo-thermal heating increases the temperature of the contracting CO core (Fig. 7, 1a). When the central density reaches  $\log \rho_c = 6.28$  and the maximum temperature in the core reaches  $\log T_{max} = 8.81$  at  $M_r = 0.05 M_\odot$ , off-center carbon ignition takes place (Fig. 7, 1b). This is because relatively high temperature activates the cooling process via neutrino emission in the CO core. The neutrino cooling efficiently removes local heat and suppresses temperature increase. The efficiency becomes greater with higher density, so for the inner region of the core, the cooling becomes more effective. However, the inner region of the core is more degenerate and thus harder to contract. On the other hand, still mildly degenerated outer region liberates gravo-thermal energy and increases its temperature, owing to the contraction by neutrino cooling. As a result, an inverse temperature gradient takes place in a degenerate core.

Since the first C burning expands and cools the central region, the burning front of this shell burning does not propagate inward and the central CO region remains. On the other hand, the second shell C burning, which takes place as the first burning dies out, propagates inward and the center of the core ignites at last (Fig. 7, 1c). The surrounding region of the second C burning shell has lower mass fraction of  $^{12}\text{C}$  owing to the first C burning. This weakens the second shell burning, resulting in a smaller expansion of the central region. This enables the second burning flame to propagate inward (Siess 2006). The propagation is caused by heat conduction from the base of the nearly stationary flame, the mean propagation speed becomes  $9.7 \times 10^{-3}$  cm/sec. Final abundances at the center of the core are shown in Table 2 in terms of mass fractions.

During the following four C flashes ( $C_{3-6}$ ), the core keeps contracting. At the ignition of the seventh C burning, the center of the core is supported only by perfectly degenerate electrons, and the central region clearly shows a temperature inversion (Fig. 7, 1d). On

the other hand, radiative pressure has a larger contribution to the total pressure both at the flame front ( $M_r=1.24 M_\odot$ ) and at the edge of the core ( $M_r=1.35 M_\odot$ ). This is due to the high temperature and low density at these regions. Figure 8 shows the evolution of the energy structure and convective region around the edge of the core. Core contraction heats the base of the surrounding helium burning shell (HeBS) and increases its luminosity. This He shell burning induces convection at the base of the HeBS (Fig. 8, 2a), and shell He burning keeps supporting the convection during the seventh and eighth C burning phases (Fig. 8, 2b & 2c).

After the end of the eighth C burning, luminosity from the shell He burning takes its maximum value owing to the temperature rise at the base of the HeBS (Fig. 8, 2d). However, soon the luminosity decreases, and the convection in a helium layer starts to be supported by escaping luminosity of C burning in the core (Fig. 8, 2e), then the growing convective region in the helium layer merges with the outer convection in the hydrogen envelope. At the moment of convective mergence, or the dredge-out episode named by Iben (1997), the temperature and density show steep drops at the edge of the core from  $\log T = 9.0 \rightarrow 6.8$  and  $\log \rho = 4.8 \rightarrow -2.4$  in a narrow mass range of  $5 \times 10^{-3} M_\odot$  (Fig. 7, 1e). Some hydrogen at the envelope are mixed into the base of the HeBS. The resulting hydrogen burning generates energy in a very high rate of  $\sim 10^{11}$  erg/sec/g (Fig. 8, 2f). The ONe core mass, which is defined by the mass coordinate of the maximum energy generation of helium burning, is  $1.347 M_\odot$  at the end of the carbon burning stage.

Since the dredge-out episode mixes CNO products with the hydrogen envelope as well as other dredge-up episodes, the surface composition changes after the convective mergence (Table 1). After completion of the dredge-out, the ONe core is surrounded by thin He shell and diffuse H envelope. In order to calculate the further evolution of the ONe core, core mass growth by shell helium burning should be considered. Thermal pulses take place at the thin helium layer in the SAGB star as in the case for lower massive AGB stars, however, simulation for the thermal pulse phase requires high cost calculation and full calculation of the phase is difficult. Moreover, as shown by Poelarends et al. (2008) for the case of the dredge-out phenomenon, not only helium but also hydrogen may be mixed with the base of the envelope and get burned out with large amount of energy production. This requires a scheme which can solve both mixing and reaction simultaneously, however, our code is not equipped with such a scheme at present. So from the end of the dredge-out episode, we assume the constant shell helium burning and avoid the numerical difficulties on core growth (see § 2.5). The radiative-zero approximation is set to be the boundary condition to the edge of the core. Since the edge structure is extremely steep, this approximation would not affect the later core evolution, especially at the central region.

### 3.2. Evolution of a contracting ONe core

In this section, we show that the evolution of an contracting ONe core can be divided into four sub-phases in terms of driving mechanisms; neutrino cooling, core mass growth, electron capture on  $^{24}\text{Mg}$  and  $^{20}\text{Ne}$ , and O+Ne deflagration. The efficiency of these mechanisms are related to evolutionary timescales which are shown in Fig. 9. The definitions of timescales are given by

$$\tau_{\text{con}} \equiv \frac{dt}{d\ln\rho_c}, \quad \tau_{\text{KH}} \equiv \frac{GM_{\text{core}}^2}{R_{\text{core}}(L + L_\nu)}, \quad \tau_{\text{growth}} \equiv \frac{dt}{d\ln M_{\text{core}}}, \quad \tau_{\text{elec}} \equiv \frac{dt}{d\ln Y_e}, \quad \tau_{\text{dyn}} \equiv \sqrt{\frac{R_{\text{core}}^3}{GM_{\text{core}}}}, \quad (26)$$

and they represents the timescale of core contraction, the Kelvin-Helmholtz timescale, the timescale of core mass growth, the timescale of electron capture, and the dynamical timescale, respectively.

#### 3.2.1. Contraction owing to neutrino cooling

From the beginning of the contraction until the central density reaches  $\log \rho_c = 9.39$ , the contraction is caused by neutrino cooling. Figure 9 shows that the time scale of contraction is close to the Kelvin-Helmholtz time scale, corresponding to the neutrino-cooling time scale. In this phase, the central temperature decreases as the entropy is radiated by thermally activated neutrino emission. As the central temperature decreases, the cooling rate of neutrino emission decreases as well. The timescale of density evolution becomes longer simultaneously.

Although electron captures on  $^{27}\text{Al}$ ,  $^{25}\text{Mg}$  and  $^{23}\text{Na}$  proceeds in this stage (Fig. 10), these reactions have just a minor effect on the density evolution. This is because, firstly, mass fractions of these nuclei are so small that reduction of electron mole fraction does not induce contraction. Secondly, thermal contributions from these reactions are smaller than neutrino cooling. Since the energy production by these electron captures is small, convection and thus convective URCA cooling as described in Ritossa et al. (1999) does not affect our calculation.

#### 3.2.2. Contraction owing to core mass growth

As the core mass increases, the central pressure, which is required to support the core, and thus the central density increase as well. While the efficiency of neutrino cooling is suppressed by entropy reduction, the efficiency of core mass growth is independent from

core structure and becomes constant. After neutrino cooling becomes less effective than core mass growth, the timescale of core growth  $\tau_{\text{growth}}$  starts to limit the contraction timescale.

The stationary core growth forces the central density to increase in a constant rate, and the production rate of gravo-thermal energy becomes constant. Owing to this constant heating, and also owing to less effective neutrino cooling, the central temperature increases proportionally to the central density.

### 3.2.3. Contraction owing to electron captures

After the central density exceeds  $\log \rho_c = 9.88$ , core contraction is driven by electron captures and thus,  $\tau_{\text{elec}}$  starts to rule the evolution time scale. The contraction time scale decreases with increasing density owing to the increasing electron capture rate. Soon core growth becomes negligible since  $\tau_{\text{elec}}$  becomes much smaller than  $\tau_{\text{growth}}$ . After that the core mass is frozen and is considered as the critical core mass for an ECSN,  $M_{\text{EC}}$ . For a  $10.8 M_{\odot}$  model,  $M_{\text{EC}}$  is  $1.366 M_{\odot}$ .

Figure 4 shows that the central temperature increases with the central density more steeply in this core growth stage. The increase of temperature is due to heating via electron captures and the main reaction sequence is  $^{24}\text{Mg} \rightarrow ^{24}\text{Na} \rightarrow ^{24}\text{Ne}$  at that time. Electron capture on  $^{24}\text{Mg}$  forms an excited  $^{24}\text{Na}^*$  as a daughter nuclei. When this  $^{24}\text{Na}^*$  decays to the ground state,  $\gamma$ -ray accompanies and heats surroundings. Owing to this additional heating, the electron capture on  $^{24}\text{Mg}$  becomes exothermic. Moreover, both  $^{24}\text{Na}^*$  and  $^{24}\text{Na}$  at the ground state can capture another electron with lower threshold density than the one of  $^{24}\text{Mg}$ . Therefore, electron capture on  $^{24}\text{Mg}$  results in double-electron capture and releases large amount of heat. It is noteworthy that the second daughter nuclei  $^{24}\text{Ne}$  becomes the dominant products of electron capture on  $^{24}\text{Mg}$  (Fig. 10). As a result, the amount of  $\nabla_{\text{rad}}$  becomes sufficiently large compared to  $\frac{\phi}{\delta} \nabla_{\mu}$ , and the central region is fully mixed by convection. The growing convection supplies fresh  $^{24}\text{Mg}$  to the center where electrons are quickly captured and the electron mole fraction decreases in the whole convective region. In accordance with the discussion by Miyaji et al. (1980), convective URCA by  $^{24}\text{Mg}$ - $^{24}\text{Ne}$  does not take place in this phase, though the reaction drives convection. This is because the threshold density of  $\beta^-$ -decay for the daughter nucleus  $^{24}\text{Ne}$  is  $\sim 10^8 \text{ g/cm}^3$  and is too small to occur in this phase. While minor electron capture nuclei, such as  $^{23}\text{Na}$  and  $^{29}\text{Si}$ , can induce convective URCA in this phase, the averaged energy loss by these reactions are reasonably smaller than heating by electron capture on  $^{24}\text{Mg}$ , and thus this process can be negligible.

After the central density reaches  $\log \rho_c = 10.3$ ,  $^{20}\text{Ne}$  starts to capture electrons (Fig. 10). This electron capture keeps driving convection as well as  $^{24}\text{Mg}$ . The time scale of the evolution becomes shorter than the one of convection, and partially mixing allows a gradient of  $X(^{20}\text{Ne})$  to exist in the central region. However, since  $^{20}\text{Ne}$  has a large mass fraction of  $\sim 0.4$ , until the commencement of Ne+O deflagration, the fuel is not consumed and the reaction continues to heat the core.

#### 3.2.4. O+Ne deflagration

When the central temperature reaches  $\log T_c = 9.2$ , O+Ne burning takes place at the center and the central temperature rises in a very short time scale. Since reaction rates of the nuclear burning highly depend on the temperature, thermal runaway takes place in the extremely degenerate region. While the temperature steeply increases at the moment of the ignition, the variance of the pressure and density becomes small. When the central temperature exceeds  $5 \times 10^9$  K, the NSE composition is assumed to be achieved.

At the boundary of the NSE region and the surrounding ONe region, there must be a negative steep gradient of entropy as a result of the O+Ne burning, and convection must exist. In our calculation, heat transportation by convection is solved (see § 2.6), and the resulting heating at the base of the ONe region becomes more efficient than the one of electron captures on neon and magnesium. The heating increases the temperature, soon the O+Ne burning ignites and the NSE is achieved. Top panels of Fig. 11 show the evolution of temperature distribution. The location of the steep temperature gradient is identical to the burning front and propagates outward. The propagation velocity,  $\sim 1.0 \times 10^3$  km/sec, becomes smaller than the sound velocity. In other words, the NSE region extends outward in mass by the O+Ne deflagration.

In the NSE region, electron capture reactions on both free-protons and heavy nuclei take place (Juodagalvis et al. 2010). The reduction of the electron mole fraction affects the dynamical evolution of the core. Contrary to electron captures on  $^{24}\text{Mg}$  and  $^{20}\text{Ne}$ , the electron capture in the NSE region becomes endothermic reaction. This is due to the global compositional change in the NSE composition; unstable neutron rich isotopes are preferable to exist in the lower  $Y_e$  environment, and thus reduction of  $Y_e$  causes the free energy to be restored in terms of nuclear binding energy. Because of the cooling, the positive entropy gradient appears in the NSE region. The center of the core becomes convectively stable.

The ONe core has been strongly bound by gravity and has a binding energy of  $-6.534 \times 10^{51}$  erg and a total energy of  $-5.791 \times 10^{50}$  erg at the commencement of O+Ne ignition.



While energy injection by the O+Ne burning is too small to disrupt the whole star, fast reduction of electrons in the NSE region accelerates core contraction. As a result of both energy injection and electron reduction, the contraction timescale of the core slowly decrease during propagation of the NSE region. After  $2.36 \times 10^{-1}$  sec from the ignition at the center of the core, the central density reaches  $\log \rho_c = 11.0$ , the deflagration front reaches  $M_{\text{NSE}} = 0.12 M_{\odot}$  and  $r_{\text{NSE}} = 1.51 \times 10^{-4} R_{\odot}$ , the binding energy and total energy of the core becomes  $-7.739 \times 10^{51}$  erg and  $-9.158 \times 10^{50}$  erg, respectively.

### 3.3. Parameter dependences on $M_{\text{EC}}$

In order to investigate the uniqueness of the critical core mass for ECSNe,  $M_{\text{EC}}$ , in various situations, additional test calculations on ONe core contraction are done with different settings. As an initial condition, ONe cores of 1.346, 1.332, and 1.288  $M_{\odot}$  are taken to be formed in SAGB stellar models of 10.8, 10.6, and 10.4  $M_{\odot}$ . For each ONe core, later contraction phase is calculated with three different rates of core mass growth of  $1.0 \times 10^{-5}$ ,  $1.0 \times 10^{-6}$ , and  $1.0 \times 10^{-7} M_{\odot}/\text{yr}$  and with or without the Coulomb correction for electron captures. Results are shown in Fig. 12.

Core masses at the end of calculations were taken as  $M_{\text{EC}}$  for each model, however, calculations were stopped for several models owing to numerical difficulties during its electron capture phase. This is due to convective URCA processes of minor nuclei such as  $^{23}\text{Na}$  and  $^{29}\text{Si}$  (see § 4.2 for discussion). For these models, we took core masses at the emergence of convection as  $M_{\text{EC}}$ . Because the contraction timescale steeply decreases after electron capture on  $^{24}\text{Mg}$  starts, and the central convection is driven by this reaction, this procedure would cause small errors on our results. For instance, the core growth after the emergence of central convection for  $M_{\text{ini}} = 10.8 M_{\odot}$  with standard settings is  $0.002 M_{\odot}$ .

The mean value of our results with the Coulomb correction is  $1.367 M_{\odot}$ . We estimate the uncertainty of  $M_{\text{EC}}$  of about  $\pm 0.005$ , taking into account the error from the procedure of determination of  $M_{\text{EC}}$  and the variances of the results. When the uncertainties which comes from the C burning phase are considered, the uncertainty should increase in total. We assume that the amount of this uncertainty is as large as one comes from later stages of evolution. Thus the uncertainty of our result is about  $\pm 0.01 M_{\odot}$  in total.

## 4. Discussions and Conclusions

### 4.1. The critical core mass for ECSNe

In our calculation,  $M_{\text{EC}}$  is  $1.367 M_{\odot}$  with a relatively small error of  $\pm 0.01 M_{\odot}$ , and is consistent with the result by Nomoto (1987),  $M_{\text{EC}} = 1.375 M_{\odot}$ . This result supports the idea that the critical core mass for ECSNe exists uniquely. I.e., in a critical object with the Chandrasekhar mass with given compositions, the central density can be represented only by the core mass,  $\rho_c = \rho_c(M_{\text{core}})$ . Therefore, the critical mass for ECSNe should be uniquely determined by solving the relation of  $\rho_{24\text{Mg}} = \rho_c(M_{\text{EC}})$ , where  $\rho_{24\text{Mg}}$  is the threshold density for electron capture on  $^{24}\text{Mg}$ .

Our result shows that inclusion of the Coulomb correction increases  $\rho_{24\text{Mg}}$  by  $\sim 10\%$  and increases  $M_{\text{EC}}$  as well. Also both faster and slower core growth may increase  $M_{\text{EC}}$ . However, these effects are smaller than the numerical uncertainties and the detailed quantitative analysis is difficult. This is because, with these critical objects, even a tiny difference in a physical quantity can cause an important change in the results. For instance, change in temperature distribution will cause a change in  $M_{\text{EC}}$ . It is difficult to uniquely determine the distribution of temperature, because the temperature of degenerate electrons is almost independent of the dynamical structure. Thus the temperature should be determined only by nuclear reactions, which relatively have larger uncertainties. The critical masses for  $10.6 M_{\odot}$  models show larger values than the other two initial masses. This may be due to the different distribution of temperature and chemical compositions.

### 4.2. Convective URCA by minor electron capture nuclei

When electron capture on  $^{24}\text{Mg}$  drives convection, convective URCA process is induced by minor electron capture nuclei such as  $^{23}\text{Na}$  and  $^{29}\text{Si}$ . In a central convective region, daughter nuclei, which are formed at the center of the core, are mixed with outer less dense region. Sometimes the density at the outer edge of the convective region is much less than the threshold densities for  $\beta^-$ -decays of these nuclei. In such cases, reaction rates of  $\beta^-$ -decays become significantly large, and this results large energy loss only at the edge of the convection. Some of our models are stopped by numerical difficulties caused by this energy loss.

However, this behavior seems unphysical, and more slow reactions will occur in reality. This is because such a large energy loss should immediately stop the convective mixing around the region, and mass fractions of these nuclei are so small that durations of these

reactions should be limited in a non-convective environment. Therefore, if small fractions of unstable  $\beta^-$ -decay nuclei are mixed into less dense regions, the resulting endothermic reaction will stop immediately and have minor effects on the whole evolution. We expect that the convective URCA process during the electron capture phase will not affect the later evolution of an ONe core as shown in the  $10.8 M_\odot$  model. To proof this statement, it is required to solve the coupling of convective mixing, nuclear reactions, and a stellar structure simultaneously.

### 4.3. Deflagration and core-collapse

Figure 9 shows that the contraction timescale  $\tau_{\text{con}}$  is longer than the dynamical timescale  $\tau_{\text{dyn}}$  even at the end of calculation. Such quasi-static contraction will be altered into dynamical collapse during the deflagration phase, and thus, the core-collapse in an ECSN is caused by electron captures in the NSE region after the initiation of O+Ne deflagration, rather than by electron captures on  $^{24}\text{Mg}$  and  $^{20}\text{Ne}$ . In order to provide a plausible progenitor model for an ECSN, the deflagration phase should be considered carefully because propagation of the deflagration front and both energy generation and electron captures in the NSE region can affect the core evolution importantly.

The obtained deflagration velocity  $1.6 \times 10^3$  km/sec at the end of the calculation ( $\rho_c = 10^{11}$  g/cm<sup>3</sup>) is consistent with a velocity  $\sim 10^3$  km/sec as in Miyaji et al. (1980). On the other hand, the extension of the NSE region,  $0.12 M_\odot$ , is smaller than  $0.354 M_\odot$  by Miyaji et al. (1980) and  $\sim 0.3 M_\odot$  by Nomoto (1987), in which the same assumptions for convective energy transportation and electron capture rates are taken. This is due to a different treatment of electron captures in the NSE region. Both Miyaji et al. (1980) and Nomoto (1987) assumed that only free-protons can capture electrons in the NSE compositions, and thus electron capture rates at low  $Y_e$  environment with extremely low proton fractions become much smaller than ours, which takes into account electron captures by neutron rich nuclei (Juodagalvis et al. 2010). In order to confirm the effect of electron captures on neutron-rich nuclei, we calculate the deflagration phase taking into account electron capture only by free-protons in NSE compositions. The resulting propagation of the NSE front is shown in Fig. 13. Comparing with the case of full electron captures, contraction becomes slower owing to smaller reduction of electrons. Then the duration of contraction becomes longer, and the flame front propagates far from the center at the end of the calculation even though the flame front has a smaller mean velocity of  $8.4 \times 10^2$  km/sec. Since the explosion as an ECSN is triggered by neutrino heating (Kitaura et al. 2006) and the efficiency is affected by the density profile, a central concentrated density profile in our calculation would affect

its explosion and the inclusion of electron captures by neutron-rich nuclei will be important.

#### 4.4. Constraints by mass loss

It is considered that not all of SAGB stars end up as ECSNe because of intense mass loss during SAGB phase. As the core increases its mass, the outer envelope is lost by this mass loss. This limits the duration of SAGB phase, and if the core mass is less than  $M_{\text{EC}}$  at the end of SAGB phase, the star ends up as an ONe WD. Therefore the ratio  $\xi \equiv \dot{M}_{\text{core}}/|\dot{M}_{\text{env}}|$  is important to determine stellar fates.

The minimum  $\xi$ , with which a star becomes an ECSN just before the star completely loses its envelope, can be defined as

$$\xi_{\text{crit}} = \frac{M_{\text{EC}} - M_{\text{core}}^{\text{ini}}}{M_{\text{tot}}^{\text{ini}} - M_{\text{EC}}} \quad (27)$$

where  $M_{\text{core}}^{\text{ini}}$  and  $M_{\text{tot}}^{\text{ini}}$  represent an ONe core mass and a total mass at the beginning of SAGB phase. When an actual  $\xi$  for a SAGB star is larger than  $\xi_{\text{crit}}$ , the star ends up as an ECSN, and vice versa. If core growth rates are specified by certain simulations, this prescription becomes identical to the definition of the critical mass loss rate  $|\dot{M}_{\text{env,crit}}|$ , thus

$$|\dot{M}_{\text{env,crit}}| \equiv \xi_{\text{crit}}^{-1} \dot{M}_{\text{core}}, \quad (28)$$

and the star with  $|\dot{M}_{\text{env}}| \leq |\dot{M}_{\text{env,crit}}|$  can become an ECSN.

$\xi_{\text{crit}}$  becomes  $2.41 \times 10^{-3}$ ,  $4.01 \times 10^{-3}$ , and  $9.25 \times 10^{-3}$  for 10.8, 10.6, and 10.4  $M_{\odot}$  models respectively. Because of large uncertainties on both  $\dot{M}_{\text{core}}$  and  $\dot{M}_{\text{tot}}$ , current estimate of  $\xi$  is highly uncertain. Here, according to the results by Poelarends et al. (2008), we limit the range of  $\xi$  as  $2.54 \times 10^{-3}$ - $1.80 \times 10^{-2}$ . This estimate includes wide ranges of mass loss rates, initial masses, and thus mass growth rates, and the minimum value will be too small to be applied to the most massive SAGB stars in our calculation. Even from this crude estimate, our model of a 10.8  $M_{\odot}$  star is plausible for the progenitor of an ECSN. This conclusion will be robust if the inclusion of overshooting reduces the total mass by  $\sim 2 M_{\odot}$  and rises  $\xi_{\text{crit}}$  to  $3.13 \times 10^{-3}$ .

#### 4.5. Conclusions

Stellar evolution for the most massive SAGB stars with solar abundances were calculated in this work, and we provided progenitor models for ECSNe with detailed evolutionary calculation for the first time.

In such a star, nuclear burnings of hydrogen, helium, and carbon take place step by step, then a core mainly made of oxygen and neon forms. The ONe core, which is supported by degenerate electron gas, contracts due to neutrino cooling, core mass growth by the surrounding shell helium burning, and reduction of electron mole fraction by electron capture reactions. When the central temperature rises high enough to ignite oxygen, O+Ne deflagration takes place and NSE is achieved in the region. Although the nuclear burning heats the region, the released energy is too small to explode the highly gravitationally bound core. As electron capture reactions on neutron-rich nuclei as well as on free protons accelerate the core contraction, the deflagration front propagates outward. The core will continue to contract up to the formation of a proto-neutron star. The fate will be a weak type II SN.

In our results, the critical mass for ECSNe,  $M_{\text{EC}}$ , is  $1.367 M_{\odot}$  with a relatively small uncertainty of about  $\pm 0.01 M_{\odot}$ , and we showed the uniqueness of the value under various initial core masses and various core growth rates. The uncertainty may come from the computational difficulties on the physically critical object as discussed in § 4.1. Inclusion of the Coulomb correction may increase  $M_{\text{EC}}$ , however, the effect is smaller than the numerical uncertainties.

Inclusion of minor intermediate mass nuclei such as  $^{29}\text{Si}$ ,  $^{23}\text{Na}$ ,  $^{25}\text{Mg}$ , and  $^{27}\text{Al}$  does not affect the core evolution and thus  $M_{\text{EC}}$ . Though convective URCA process by these nuclei sometimes cause numerical difficulties in an electron capture phase, this process will have minor effect on the whole evolution.

Since the ONe core keeps contracting quasi-statically even during the deflagration phase, the core evolution is importantly affected by propagation of the deflagration front and electron capture in the NSE region. We showed that the assumption of electron capture only by free-protons leads slower contraction and electron captures on neutron-rich nuclei should be treated.

Owing to intense mass loss during SAGB phase, not all of our models may end up as ECSNe. Accurate estimates for the core growth rate and the mass loss rate are difficult and further investigations are still needed on this topic. However, even under the most severe condition which is taken from the work by Poelarends et al. (2008), our  $10.8 M_{\odot}$  model is plausible for a progenitor model of an ECSN.

We would like to thank Andrius Juodagalvis, Karlheinz Langanke, and Gabriel Martínez-Pinedo for providing electron capture rates for the NSE compositions. We are grateful to Ken'ichi Nomoto for his useful discussions. This work is supported in part by JSPS KAKENHI Grant Numbers 20540284, 20041005, 20105004.

## REFERENCES

- Böhm-Vitense, E. 1958, *Z. Astrophys.*, 46, 108
- Botticella, M. T., et. al. 2009, *MNRAS*, 398, 1041
- Couch, R. G., & Loumos, G. L. 1974, *ApJ*, 194, 385
- Couch, R. G., & Arnett, W. D. 1975, *ApJ*, 196, 791
- DeWitt, H. E., Graboske, H. C., & Cooper, M. S. 1973, *ApJ*, 181, 439
- García-Berro, E., & Iben, I., Jr. 1994, *ApJ*, 434, 306
- García-Berro, E., Ritossa, C., & Iben, I., Jr. 1997, *ApJ*, 485, 765
- Gil-Pons, P., Suda, T., Fujimoto, M. Y., & García-Berro, E. 2005, *A&A*, 433, 1037
- Gil-Pons, P., Gutiérrez, J., & García-Berro, E. 2007, *A&A*, 464, 667
- Gutiérrez, J., García-Berro, E., Iben, I., Jr., Isern, J., Labay, J., & Canal, R. 1996, *ApJ*, 459, 701
- Gutiérrez, J., Canal, R., & García-Berro, E. 2005, *A&A*, 435, 231
- Kato, S. 1966, *Publ. Astron. Soc. Japan*, 18, 374
- Kitaura, F. S., Janka, H. -Th., & Hillebrandt, W. 2006, *A&A*, 450, 345
- Herwig, F. 2000, *A&A*, 360, 952
- Hashimoto, M., Iwamoto, K., & Nomoto, K. 1993, *ApJ*, 414, L105
- Heger, A., Langer, N., & Woosley, S. E. 2000, *ApJ*, 528, 368
- Hirschi, R., Meynet, G., & Maeder, A. 2004, *A&A*, 425, 649
- Iben, I., Jr. 1978, *ApJ*, 226, 996
- Iben, I., Jr., Ritossa, C., & García-Berro, E. 1997, *ApJ*, 489, 772
- Janka, H. -Th., Hanke, F., Hüdepohl, L., Marek, A., Müller, B., & Obergaulinger, M. 2012, submitted to *Prog. Theor. Exp. Phys.*; arXiv1211.1378
- Juodagalvis, A., Langanke, K., Hix, W. R., Martínez-Pinedo, G., & Sampaio, J. M. 2010, *Nucl. Phys. A*, 848, 454

- Limongi, M., & Chieffi, A. 2006, *ApJ*, 647, 483
- Miyaji, S., Nomoto, K., Yokoi, K., & Sugimoto, D. 1980, *Publ. Astron. Soc. Japan*, 32, 303
- Miyaji, S., & Nomoto, K. 1987, *ApJ*, 318, 307
- Nomoto, K., Sparks, W. M., Fesen, R. A., Gull, T. R., Miyaji, S., & Sugimoto, D. 1982, *Nature*, 299, 803
- Nomoto, K. 1984, *ApJ*, 277, 791
- Nomoto, K. 1987, *ApJ*, 322, 206
- Nomoto, K., & Hashimoto, M. 1988, *Phys. Rep.*, 163, 13
- Pastorello, A., et al. 2006, *MNRAS*, 370, 1752
- Pastorello, A., et al. 2009, *MNRAS*, 394, 2266
- Poelarends, A. J. T., Herwig, F., Langer, N., & Heger, A. 2008, *ApJ*, 675, 614
- Pumo, M. L., Turatto, M., Botticella, M. T., Pastorello, A., Valenti, S., Zampiepi, L., Benetti, S., Cappellaro, E., & Patat, F. 2009, *ApJ*, 705, L138
- Ritossa, C., García-Berro, E., & Iben, I., Jr. 1996, *ApJ*, 460, 489
- Ritossa, C., García-Berro, E., & Iben, I., Jr. 1999, *ApJ*, 515, 381
- Siess, L. 2006, *A&A*, 448, 717
- Siess, L. 2007, *A&A*, 476, 893
- Siess, L. 2009, *A&A*, 497, 463
- Siess, L. 2010, *A&A*, 512, A10
- Spruit, H. C. 1992, *A&A*, 253, 131
- Turatto, M., et al. 1998, *ApJ*, 498, L129
- Umeda, H., & Nomoto, K. 2008, *ApJ*, 673, 1014
- Umeda, H., Yoshida, T., & Takahashi, K. 2012, *Prog. Theor. Exp. Phys.*, 01, A302
- Unno, W. 1967, *Publ. Astron. Soc. Japan*, 19, 140
- Yoshida, T., & Umeda, H. 2011, *MNRAS*, 412, L78

Yoshida, T., Okita, S., & Umeda, H. 2013, submitted to MNRAS

Wanajo, S., Janka, H. -Th., & Müller, B. 2011, ApJ, 726, L15

Wanajo, S., Janka, H. -Th., & Müller, B. 2013, submitted to ApJ; arXiv1302.0929



Table 1: Surface abundances at three different stages of ZAMS, the 1st dredge-up, and the dredge-out.

	$^1\text{H}$	$^3\text{He}$	$^4\text{He}$	$^{12}\text{C}$	$^{13}\text{C}$	$^{14}\text{N}$	$^{15}\text{N}$	$^{16}\text{O}$
ZAMS	$7.059 \times 10^{-1}$	$8.946 \times 10^{-5}$	$2.740 \times 10^{-1}$	$3.196 \times 10^{-3}$	$3.847 \times 10^{-5}$	$1.164 \times 10^{-3}$	$4.599 \times 10^{-6}$	$1.011 \times 10^{-2}$
1DUP	$6.778 \times 10^{-1}$	$4.566 \times 10^{-5}$	$3.021 \times 10^{-1}$	$1.876 \times 10^{-3}$	$9.926 \times 10^{-5}$	$3.704 \times 10^{-3}$	$1.869 \times 10^{-6}$	$8.893 \times 10^{-3}$
DOUT	$5.729 \times 10^{-1}$	$3.592 \times 10^{-5}$	$4.050 \times 10^{-1}$	$3.105 \times 10^{-3}$	$9.049 \times 10^{-5}$	$4.933 \times 10^{-3}$	$1.490 \times 10^{-6}$	$7.837 \times 10^{-3}$
	$^{17}\text{O}$	$^{18}\text{O}$	$^{21}\text{Ne}$	$^{22}\text{Ne}$	$^{23}\text{Na}$	$^{25}\text{Mg}$	$^{26}\text{Mg}$	
ZAMS	$4.097 \times 10^{-6}$	$2.284 \times 10^{-5}$	$4.350 \times 10^{-6}$	$1.372 \times 10^{-4}$	$3.519 \times 10^{-5}$	$7.131 \times 10^{-5}$	$8.178 \times 10^{-5}$	
1DUP	$1.168 \times 10^{-5}$	$1.504 \times 10^{-5}$	$4.344 \times 10^{-6}$	$1.137 \times 10^{-4}$	$5.969 \times 10^{-5}$	$6.554 \times 10^{-5}$	$8.776 \times 10^{-5}$	
DOUT	$1.064 \times 10^{-5}$	$2.246 \times 10^{-4}$	$3.906 \times 10^{-6}$	$4.634 \times 10^{-4}$	$7.974 \times 10^{-5}$	$5.717 \times 10^{-5}$	$1.032 \times 10^{-4}$	

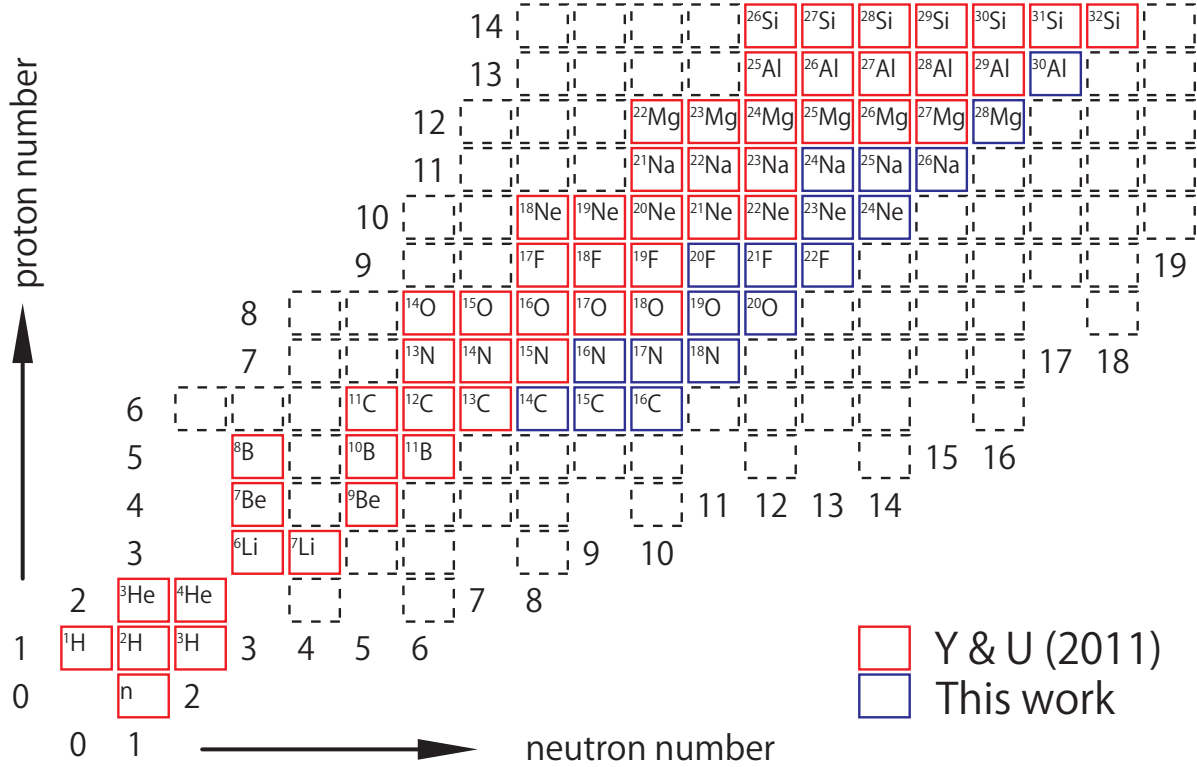


Fig. 1.— Nuclei with proton number less than 14 that are included in our calculation. Eighteen blue nuclei are newly included and 300 in total are taken into consideration, while red nuclei had been taken into account in our previous paper (Y&U11).

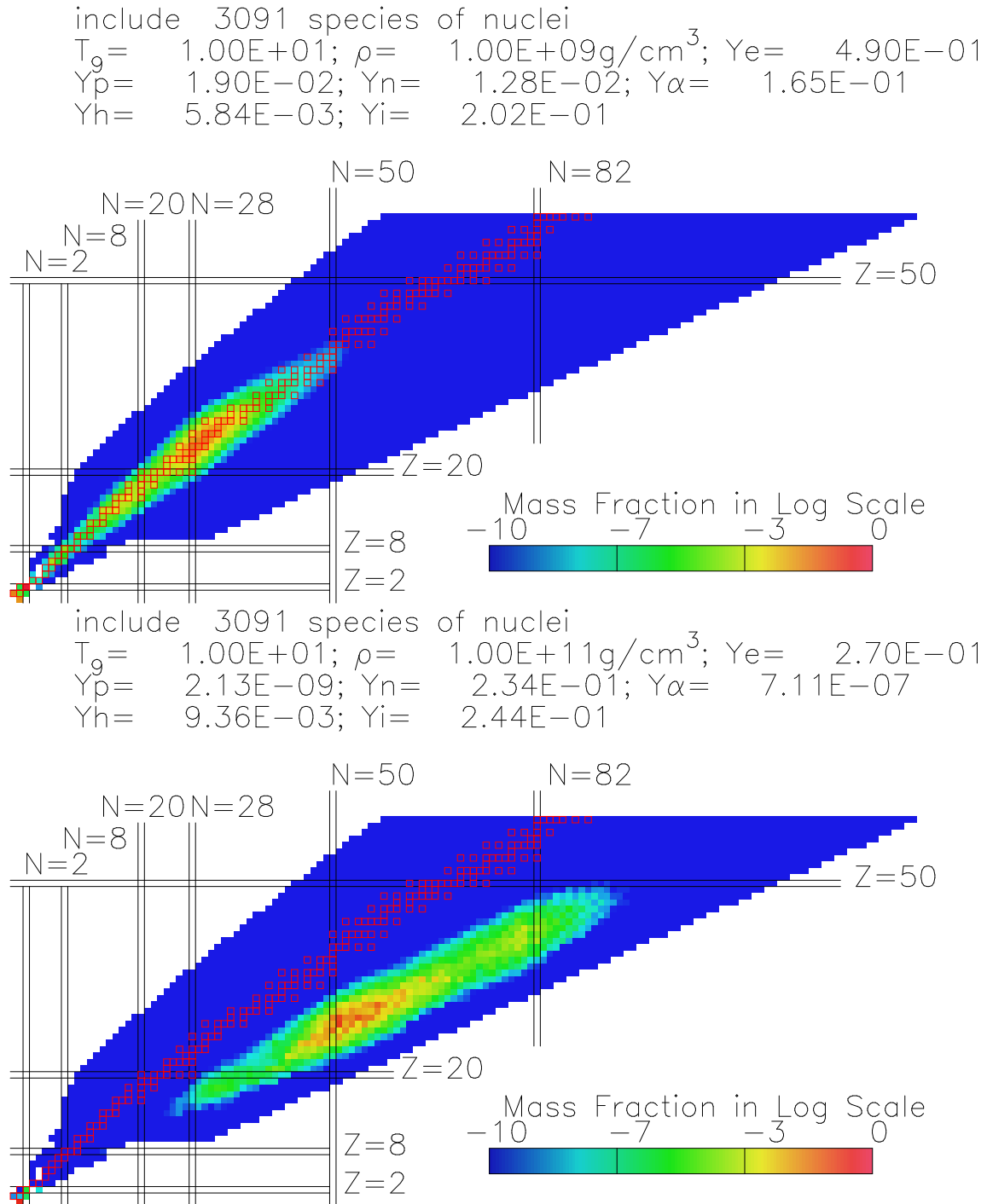


Fig. 2.— The NSE composition on (N, Z) plane in the cases of (temperature [10<sup>9</sup> K], density [g/cm<sup>3</sup>], electron mole fraction)=(10.0, 10<sup>9</sup>, 0.49) and (10.0, 10<sup>11</sup>, 0.27). Blue region shows the region of considered 3091 nuclei and red boxes represent stable nuclei. Color contours show the mass fraction distribution.

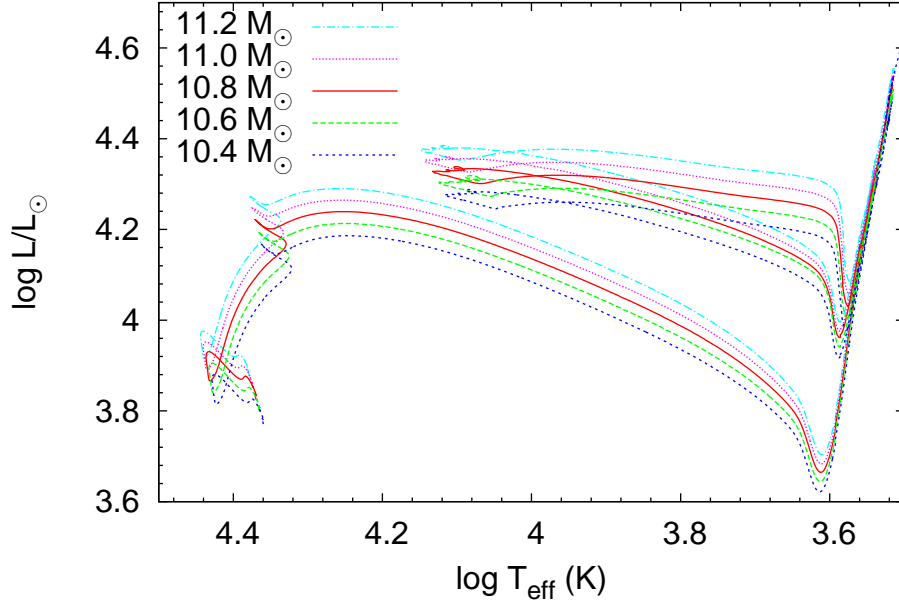


Fig. 3.— Evolution of  $\sim 11 M_{\odot}$  models in the HR diagram.

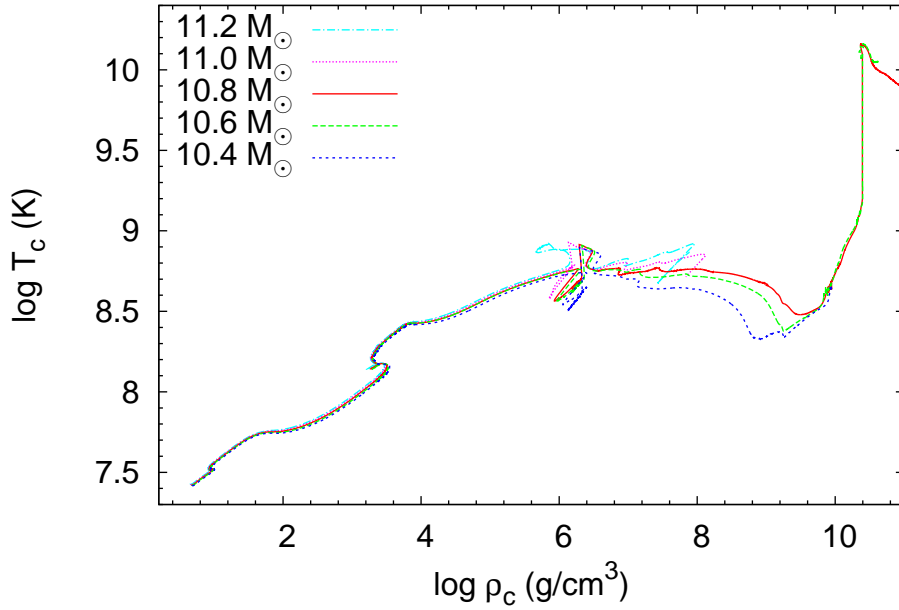


Fig. 4.— Evolution of  $\sim 11 M_{\odot}$  models in the central density-temperature plane.

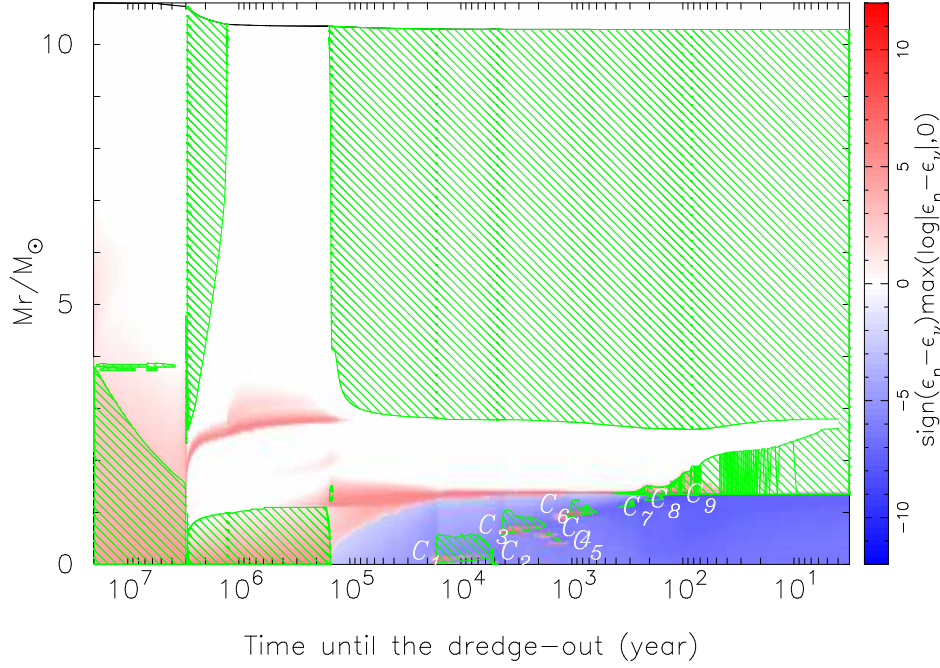


Fig. 5.— The time evolution of convective regions of a  $10.8 M_{\odot}$  model until completion of the dredge-out. Convective regions are shown in green hatched region in the figure, and log scaled net nuclear energy generation is shown in color.

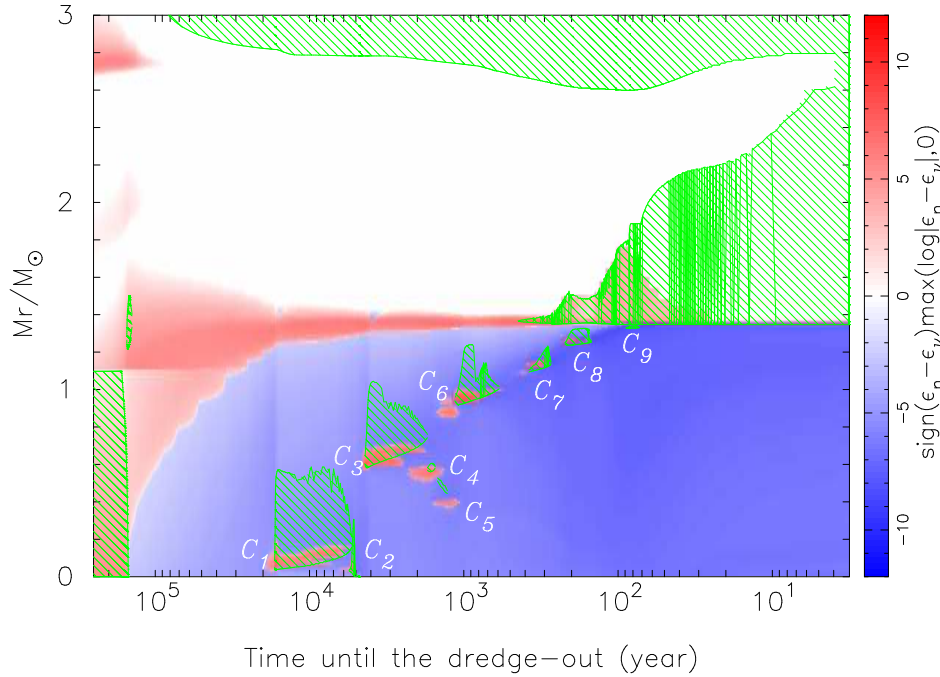


Fig. 6.— Same as Fig. 5 but expanded on a off-center C burning phase.

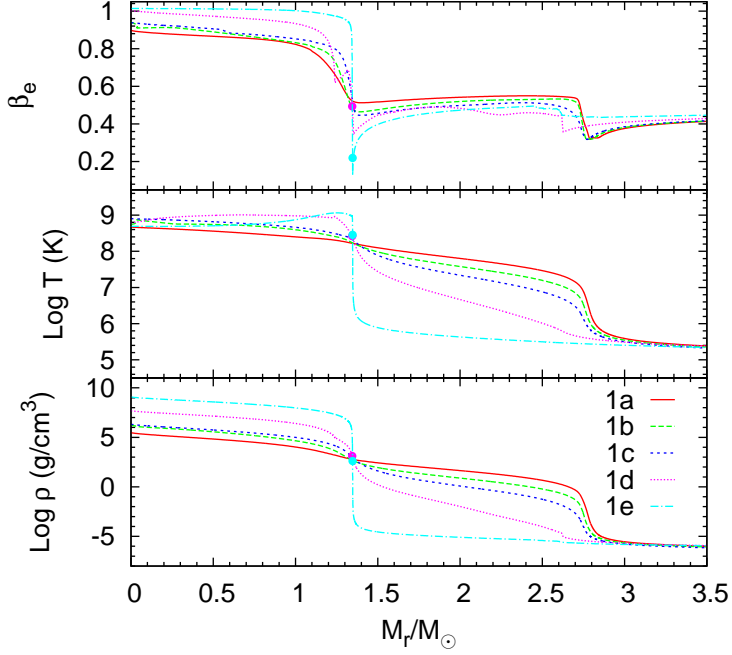


Fig. 7.— Structure evolution in terms of electron pressure fraction (top), temperature (middle), and density (bottom) as functions of mass coordinate at five different stages: disappearance of convective core helium burning (1a), commencement of the first shell carbon burning (1b), ignition at the center of the core (1c), ignition of the eighth C burning (1d), and occurrence of the dredge-out (1e). Points show the locations of the base of the HeBS for (1d) and (1e).

Table 2: Central abundance at the end of core carbon burning phase.

$^{16}\text{O}$	$^{20}\text{Ne}$	$^{24}\text{Mg}$	$^{23}\text{Na}$	$^{25}\text{Mg}$	$^{26}\text{Mg}$	$^{27}\text{Al}$
$4.783 \times 10^{-1}$	$4.074 \times 10^{-1}$	$4.255 \times 10^{-2}$	$3.217 \times 10^{-2}$	$1.451 \times 10^{-2}$	$7.952 \times 10^{-3}$	$7.245 \times 10^{-3}$
$^{22}\text{Ne}$	$^{28}\text{Si}$	$^{12}\text{C}$	$^{21}\text{Ne}$	$^{30}\text{Si}$	$^{29}\text{Si}$	$^{32}\text{S}$
$2.836 \times 10^{-3}$	$2.330 \times 10^{-3}$	$1.277 \times 10^{-3}$	$8.384 \times 10^{-4}$	$3.621 \times 10^{-4}$	$3.362 \times 10^{-4}$	$1.463 \times 10^{-4}$

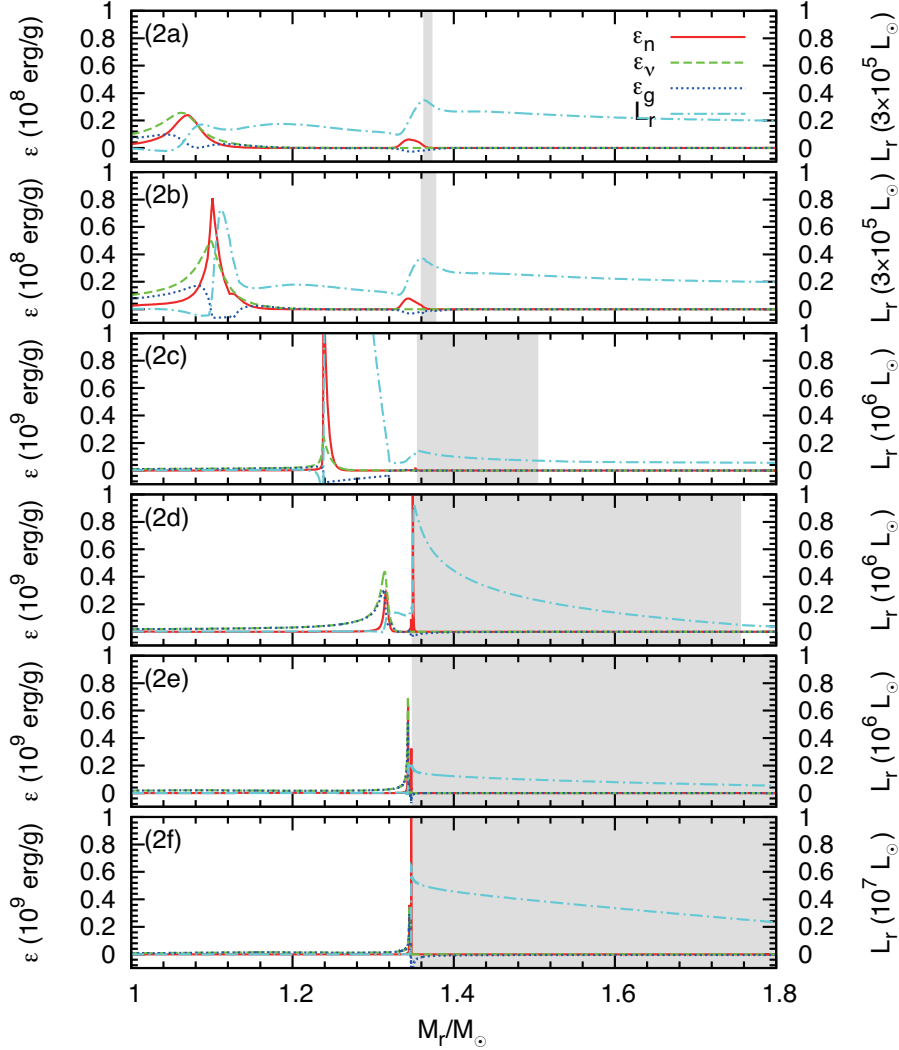


Fig. 8.— Profiles of the energy generation rates and luminosity with mass coordinate at different stages: occurrence of convection on HeBS (2a), ignition of the seventh C burning (2b), ignition of the eighth C burning (2c), shell He burning at its maximum (2d),  $6.84 \times 10^7$  yr after (2d) (2e), and occurrence of the dredge-out (2f). Different line types are the nuclear energy generation (red, solid line), the neutrino energy loss (green, dashed line) the gravo-thermal energy release (blue, dotted line), and the luminosity (cyan, dash-dotted line) respectively. Gray regions represent convective regions.

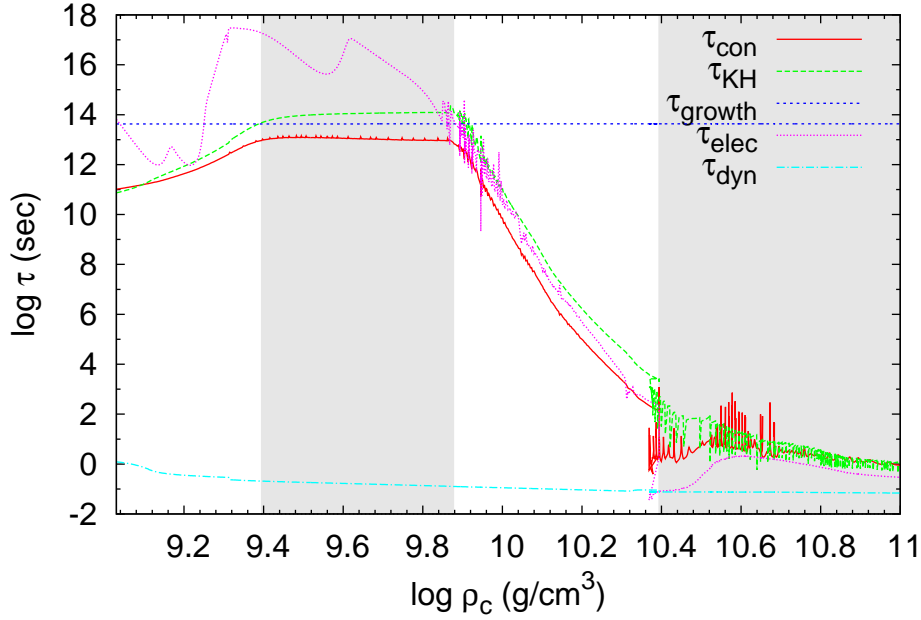


Fig. 9.— Evolution of the timescales with density at the stellar center. Different lines correspond to different timescales: timescale of core contraction  $\tau_{\text{con}}$  (red, solid line), Kelvin-Helmholtz timescale  $\tau_{\text{KH}}$  (green, long dashed line), timescale of core mass growth  $\tau_{\text{growth}}$  (blue, short dashed line), timescale of electron capture  $\tau_{\text{elec}}$  (magenta, dotted line), and dynamical timescale  $\tau_{\text{dyn}}$  (cyan, dash-dotted line). Background colors shows different sub-phases: the neutrino cooling phase ( $\log \rho_c \leq 9.39$ ), the core growth phase ( $9.39 < \log \rho_c \leq 9.88$ ), the electron capture phase ( $9.88 < \log \rho_c \leq 10.39$ ), and the deflagration phase ( $10.39 < \log \rho_c$ ).

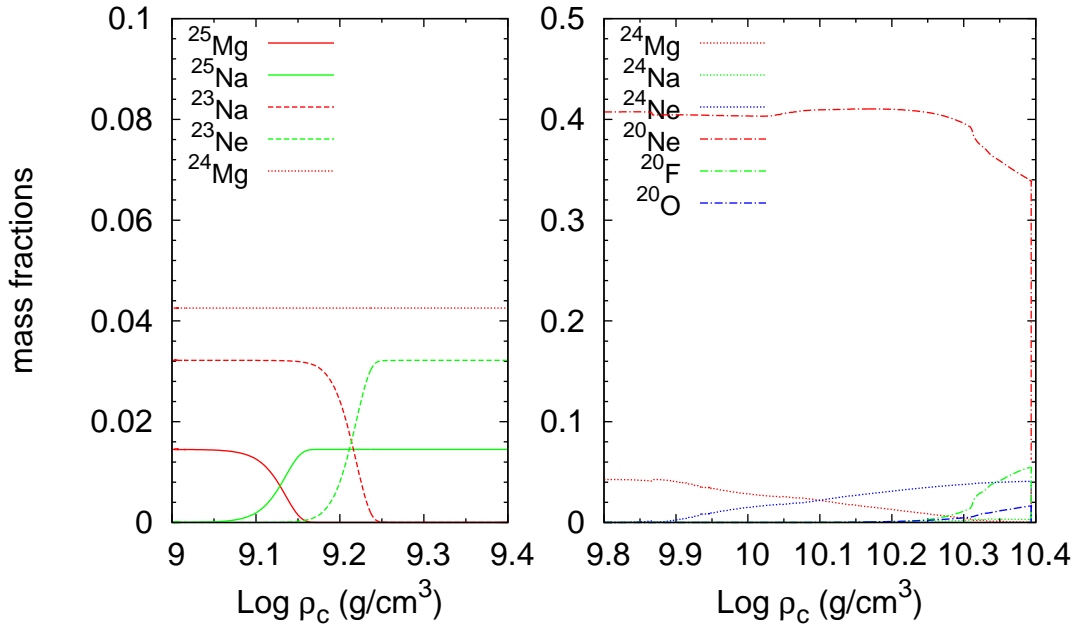


Fig. 10.— Evolution of mass fractions of electron capture nuclei at the stellar center with central density. For lower density, mass fractions of  $^{25}\text{Mg}$ ,  $^{25}\text{Na}$  (red & green, solid line),  $^{23}\text{Na}$ ,  $^{23}\text{Ne}$  (red & green, dashed line), and  $^{24}\text{Mg}$  (orange, dotted line) are shown. For higher density, mass fractions of  $^{24}\text{Mg}$ ,  $^{24}\text{Na}$ ,  $^{24}\text{Ne}$  (orange, green, & blue, dotted line) and  $^{20}\text{Ne}$ ,  $^{20}\text{F}$ ,  $^{20}\text{O}$  (orange, green, & blue, dash-dotted line) are shown.



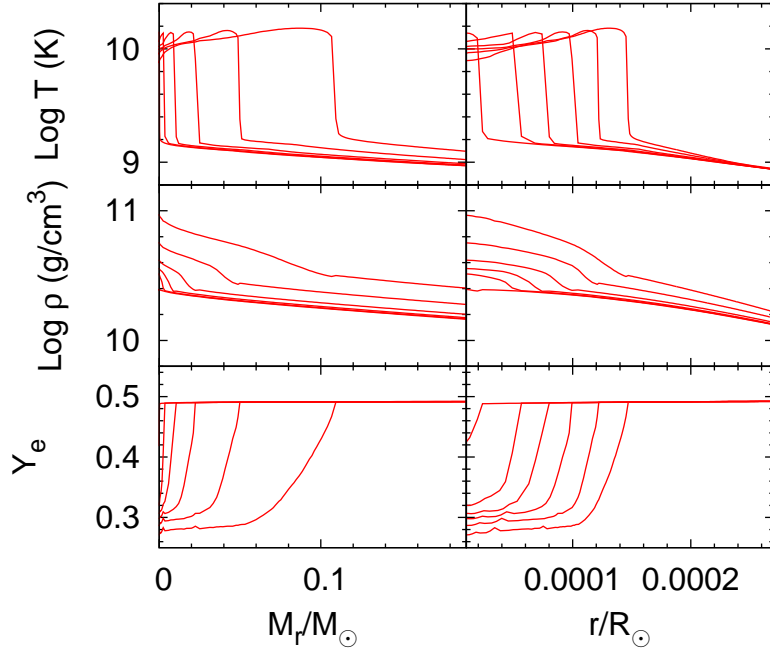


Fig. 11.— Profiles of temperature, density and electron mole fraction during O+Ne deflagration are shown as a function of both mass and radius coordinates. These profiles are taken at  $1.13 \times 10^{-2}$ ,  $5.40 \times 10^{-2}$ ,  $9.92 \times 10^{-2}$ ,  $1.49 \times 10^{-1}$ ,  $2.00 \times 10^{-1}$ , and  $2.34 \times 10^{-1}$  sec after the ignition at the center of the core.

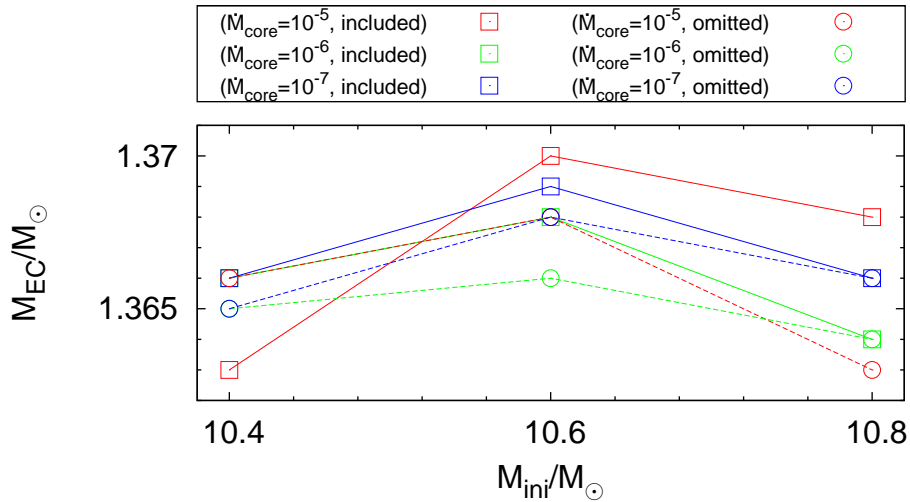


Fig. 12.— The critical core masses for ECSNe calculated with different settings. Different colors show different core growth rates and different point types show different treatments of the Coulomb correction.

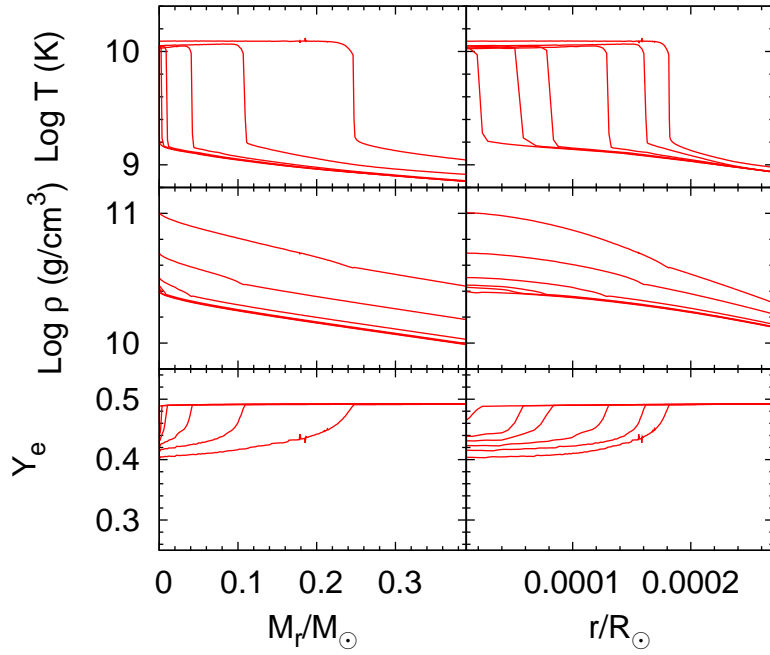


Fig. 13.— Same as Fig. 11 with electron capture rate only by free-protons. These profiles are taken at  $1.15 \times 10^{-2}$ ,  $5.56 \times 10^{-2}$ ,  $1.00 \times 10^{-2}$ ,  $2.00 \times 10^{-1}$ ,  $3.00 \times 10^{-1}$ , and  $3.58 \times 10^{-1}$  sec after the O+Ne ignition at the center of the core.